

THE STRUCTURE OF PRE-TRANSITIONAL PROTOPLANETARY DISKS. II.  
AZIMUTHAL ASYMMETRIES, DIFFERENT RADIAL DISTRIBUTIONS OF LARGE AND SMALL DUST  
GRAINS IN PDS 70. \* †

J. HASHIMOTO<sup>1</sup>, T. TSUKAGOSHI<sup>2</sup>, J. M. BROWN<sup>3</sup>, R. DONG<sup>4,5</sup>, T. MUTO<sup>6</sup>, Z. ZHU<sup>4,7</sup>, J. WISNIEWSKI<sup>1</sup>, N. OHASHI<sup>8</sup>,  
T. KUDO<sup>8</sup>, N. KUSAKABE<sup>9</sup>, L. ABE<sup>10</sup>, E. AKIYAMA<sup>9</sup>, W. BRANDNER<sup>11</sup>, T. BRANDT<sup>12</sup>, J. CARSON<sup>13,11</sup>, T. CURRIE<sup>14</sup>,  
S. EGNER<sup>8</sup>, M. FELDT<sup>11</sup>, C. A. GRADY<sup>15,16</sup>, O. GUYON<sup>8</sup>, Y. HAYANO<sup>8</sup>, M. HAYASHI<sup>9</sup>, S. HAYASHI<sup>8</sup>, T. HENNING<sup>11</sup>,  
K. HODAPP<sup>17</sup>, M. ISHI<sup>9</sup>, M. IYE<sup>9</sup>, M. JANSON<sup>18,11</sup>, R. KANDORI<sup>9</sup>, G. KNAPP<sup>7</sup>, M. KUZUHARA<sup>19</sup>, J. KWON<sup>20</sup>, T. MATSUO<sup>21</sup>,  
M. W. McELWAIN<sup>16</sup>, S. MAYAMA<sup>22</sup>, K. MEDE<sup>20</sup>, S. MIYAMA<sup>23</sup>, J.-I. MORINO<sup>9</sup>, A. MORO-MARTIN<sup>24,7</sup>, T. NISHIMURA<sup>8</sup>,  
T.-S. PYO<sup>8</sup>, G. SERABYN<sup>25</sup>, T. SUENAGA<sup>26</sup>, H. SUTO<sup>9</sup>, R. SUZUKI<sup>9</sup>, Y. TAKAHASHI<sup>26</sup>, M. TAKAMI<sup>27</sup>, N. TAKATO<sup>8</sup>,  
H. TERADA<sup>8</sup>, C. THALMANN<sup>28,29</sup>, D. TOMONO<sup>8</sup>, E. L. TURNER<sup>7,30</sup>, M. WATANABE<sup>31</sup>, T. YAMADA<sup>32</sup>, H. TAKAMI<sup>9</sup>,  
T. USUDA<sup>9</sup>, M. TAMURA<sup>20,9</sup>

*Draft version August 29, 2021*

ABSTRACT

The formation scenario of a gapped disk, i.e., transitional disk, and its asymmetry is still under debate. Proposed scenarios such as disk-planet interaction, photoevaporation, grain growth, anticyclonic vortex, eccentricity, and their combinations would result in different radial distributions of the gas and the small (sub- $\mu\text{m}$  size) and large (millimeter size) dust grains as well as asymmetric structures in a disk. Optical/near-infrared (NIR) imaging observations and (sub-)millimeter interferometry can trace small and large dust grains, respectively; therefore multi-wavelength observations could help elucidate the origin of complicated structures of a disk. Here we report SMA observations of the dust continuum at 1.3 mm and  $^{12}\text{CO } J = 2 \rightarrow 1$  line emission of the pre-transitional protoplanetary disk around the solar-mass star PDS 70. PDS 70, a weak-lined T Tauri star, exhibits a gap in the scattered light from its disk with a radius of  $\sim 65$  AU at NIR wavelengths. However, we found a larger gap in the disk with a radius of  $\sim 80$  AU at 1.3 mm. Emission from all three disk components (the gas and the small and large dust grains) in images exhibits a deficit in brightness in the central region of the disk, in particular, the dust-disk in small and large dust grains has asymmetric brightness. The contrast ratio of the flux density in the dust continuum between the peak position to the opposite side of the disk reaches 1.4. We suggest the asymmetries and different gap-radii of the disk around PDS 70 are potentially formed by several (unseen) accreting planets inducing dust filtration.

*Subject headings:* planetary systems — protoplanetary disks — stars: individual (PDS 70) — stars: pre-main sequence — submillimeter: general — polarization

\*BASED ON DATA COLLECTED AT THE SUBARU TELESCOPE, WHICH IS OPERATED BY THE NATIONAL ASTRONOMICAL OBSERVATORY OF JAPAN.

†THE SUBMILLIMETER ARRAY IS A JOINT PROJECT BETWEEN THE SMITHSONIAN ASTROPHYSICAL OBSERVATORY AND THE ACADEMIA SINICA INSTITUTE OF ASTRONOMY AND ASTROPHYSICS AND IS FUNDED BY THE SMITHSONIAN INSTITUTION AND THE ACADEMIA SINICA.

<sup>1</sup> Department of Physics and Astronomy, The University of Oklahoma, 440 W. Brooks St. Norman, OK 73019 USA; jun.hashimoto@ou.edu

<sup>2</sup> College of Science, Ibaraki University, Bunkyo 2-1-1, Mito 310-8512, Japan

<sup>3</sup> Harvard-Smithsonian Center for Astrophysics, 60 Garden St., MS 78, Cambridge, MA 02138, USA

<sup>4</sup> Hubble Fellow

<sup>5</sup> Astronomy Department, University of California, Berkeley, CA 94720, USA

<sup>6</sup> Division of Liberal Arts, Kogakuin University, 1-24-2, Nishi-Shinjuku, Shinjuku-ku, Tokyo, 163-8677, Japan

<sup>7</sup> Department of Astrophysical Sciences, Princeton University, Princeton, NJ, 08544, USA

<sup>8</sup> Subaru Telescope, 650 North A'ohoku Place, Hilo, HI 96720, USA

<sup>9</sup> National Astronomical Observatory of Japan, 2-21-1 Osawa, Mitaka, Tokyo 181-8588, Japan

<sup>10</sup> Laboratoire Hippolyte Fizeau, UMR6525, Universite de Nice Sophia-Antipolis, 28, avenue Valrose, 06108 Nice Cedex 02, France

<sup>11</sup> Max Planck Institute for Astronomy, Königstuhl 17, D-69117 Heidelberg, Germany

<sup>12</sup> Astrophysics Department, Institute for Advanced Study, Princeton, USA

<sup>13</sup> Department of Physics and Astronomy, College of Charleston, 58 Coming St., Charleston, SC29424, USA

<sup>14</sup> Department of Astronomy and Astrophysics, University of Toronto, 50 St. George Street, Toronto, ON, Canada

<sup>15</sup> Eureka Scientific, 2452 Delmer, Suite 100, Oakland CA 96002, USA

<sup>16</sup> Exoplanets and Stellar Astrophysics Laboratory, Code 667, Goddard Space Flight Center, Greenbelt, MD 20771 USA

<sup>17</sup> University of Hawaii, 640 North A'ohoku Place, Hilo, HI 96720, USA

<sup>18</sup> Astrophysics Research Center, Queen's University Belfast, Belfast, UK

<sup>19</sup> Department of Earth and Planetary Sciences, Tokyo Institute of Technology, 2-12-1 Ookayama, Meguro-ku, Tokyo 152-8551, Japan

<sup>20</sup> Department of Astronomy, The University of Tokyo, Hongo 7-3-1, Bunkyo-ku, Tokyo 113-0033, Japan

<sup>21</sup> Department of Astronomy, Kyoto University, Kita-shirakawa-Oiwake-cho, Sakyo-ku, Kyoto 606-8502, Japan

<sup>22</sup> The Graduate University for Advanced Studies (SOK-ENDAI), Shonan International Village, Hayama-cho, Miura-gun, Kanagawa 240-0193, Japan

<sup>23</sup> Hiroshima University, 1-3-2, Kagamiyama, Higashi-Hiroshima 739-8511, Japan

<sup>24</sup> Department of Astrophysics, CAB - CSIC/INTA, 28850 Torrejón de Ardoz, Madrid, Spain

<sup>25</sup> Jet Propulsion Laboratory, California Institute of Technology, 4800 Oak Grove Drive, Pasadena, CA 91109, USA

<sup>26</sup> Department of Astronomical Science, Graduate University for

## 1. INTRODUCTION

It is widely believed that protoplanetary disks dissipate inside-out (c.f., Williams & Cieza 2011) and evolve into planetary systems (e.g., Hayashi, Nakazawa, & Nakagawa 1985). When an inner disk at less than  $r \sim 1$  AU begins to dissipate, thermal emission from the disk significantly decreases at near- (NIR) to mid-infrared (MIR) wavelengths corresponding to a blackbody temperature of  $\sim 100$ – $1000$  K. As a result, a deficit of flux density at  $\sim 10$   $\mu\text{m}$  appears in an object’s spectral energy distribution (SED). Such objects were first identified with the *IRAS* satellite (Strom et al. 1989) and are termed ‘transitional disks (in transition between gas-rich primordial disks and gas-poor debris disks)’ (Calvet et al. 2005; Espaillat et al. 2014). Recent high resolution and high dynamic range imaging has directly revealed gaps in the central region of disks among roughly two dozen transitional disks at NIR (e.g., Thalmann et al. 2010; Hashimoto et al. 2012; Mayama et al. 2012; Debes et al. 2013; Garufi et al. 2013; Quanz et al. 2013) and (sub)-millimeter wavelengths (e.g., Piétu et al. 2005; Brown et al. 2009; Andrews et al. 2011; Williams & Cieza 2011; Fukagawa et al. 2013; Pérez et al. 2014). Some transitional disks also show asymmetries in their dust continuum (e.g., Brown et al. 2009; Pérez et al. 2014). To explain how the gap and the asymmetry form, a number of scenarios have been proposed: disk-planet interaction (Papaloizou et al. 2007; Zhu et al. 2011; Dodson-Robinson & Salyk 2011), photoevaporation (Clarke, Gendrin, & Sotomayor 2001; Alexander, Clarke, & Pringle 2006; Alexander & Armitage 2007), grain growth (Dullemond & Dominik 2005; Birnstiel, Andrews, & Ercolano 2012), anticyclonic vortex (Regály et al. 2012), eccentricity (Kley & Dirksen 2006; Ataiee et al. 2013), and their combinations (dust filtration; radiation pressure; Rice et al. 2006; Dong et al. 2012a; Zhu et al. 2012; Pinilla, Benisty, & Birnstiel 2012; Owen 2014).

Different gap formation scenarios could result in different radial distributions of the surface density of the gas and dust grains. For instance, *disk-planet interactions* will open a gap in the disk, but will have little effect on the inner gas-disk (e.g., Zhu et al. 2011). Optically thick inner and outer disks in the optical/NIR wavelengths would be separated by an optically thin gap. *Photoevaporation* should remove almost all the gas at the inner disk quickly, leaving a gas free cavity (e.g., Alexander & Armitage 2007). A supply of fresh material from the outer disk through

mass accretion could be halted by a photoevaporative wind, resulting in remaining dust grains in the inner disk rapidly draining onto the star and creating a cavity (containing empty or optically thin materials). *Grain growth* would mainly affect the dust grains, leaving gas unaffected (e.g., Dullemond & Dominik 2005). Birnstiel, Andrews, & Ercolano (2012) demonstrate that grain growth could account for the deficit of NIR and MIR excess in the SED of transitional disks, whereas they predict large (millimeter size) dust grains still remain in the inner disk region. Another intriguing scenario generating different radial distributions could be *dust filtration* (e.g., Rice et al. 2006), whereby large dust grains are trapped at the gas-pressure-bump, while small dust grains mixed well with the gas still inflow onto the central star. *Radiation pressure* from an accreting planet (Owen 2014) can also influence its nearby environment. When a massive planet ( $\gtrsim 3\text{--}4 M_{\text{Jup}}$ ) opens a gap and has sufficient mass accretion from the outer disk, radiation pressure from the planet is expected to hold back small dust grains, allowing the dust-free gas to accrete onto the central star. On the other hand, *anticyclonic vortices* (Regály et al. 2012) and *eccentricities* (Kley & Dirksen 2006) result in asymmetric structures in the disk. Anticyclonic vortices induced at the steep gas-pressure gradient such as a ‘dead zone’ (Gammie 1996) and a gap-edge sculpted by planet(s) have a higher gas surface-density and efficiently gather dust particles into central vortices; eccentric disks formed by a massive planet create a ‘traffic jam’ of the gas and dust grains at the disk apocenter and result in steady asymmetric features.

Determining the radial and azimuthal distributions of these disk components (the gas and the small and large dust grains) are crucial to understanding the formation of gaps in these disks as well as the origin of observed asymmetries. However, transitional disks with a spatially resolved gap in all three disk components are relatively rare: AB Aur (Piétu et al. 2005; Hashimoto et al. 2011; Tang et al. 2012); RX J1604.3–2130 A (Mathews, Williams, & Ménard 2012; Mayama et al. 2012); SAO 206462 (e.g., Brown et al. 2009; Lyo et al. 2011; Garufi et al. 2013; Pérez et al. 2014); HD 142527 (e.g., Fukagawa et al. 2006; Casassus et al. 2013); Oph IRS 48 (e.g., Geers et al. 2007; Brown et al. 2012; van der Marel et al. 2013; Bruderer et al. 2014, Follette et al. in prep.).

Here we report the results of the dust continuum at 1.3 mm and  $^{12}\text{CO}$  ( $2 \rightarrow 1$ ) line emission from the pre-transitional protoplanetary disk around PDS 70 obtained with the Submillimeter Array (SMA). PDS 70 is a solar-type star with a mass of  $\sim 0.8 M_{\odot}$  at an assumed distance of 140 pc (Riaud et al. 2006). The other basic properties of PDS 70 can be found in Hashimoto et al. (2012), Dong et al. (2012b), and references therein. The PDS 70 disk exhibits a large gap with a radius of  $\sim 65$  AU at NIR wavelengths (Hashimoto et al. 2012; Dong et al. 2012b), which enables SMA observations to resolve a large gap in both dust continuum and the CO gas. In this paper, we discuss the gap formation scenario and the possible origin of fine structures in the disk around PDS 70.

## 2. OBSERVATIONS AND RESULTS

PDS 70 (14:08:10.125,  $-41:23:52.81$ ; Cutri et al. 2013) was observed with the Submillimeter Array in three con-

Advanced Studies (Sokendai), Tokyo 181-8588, Japan

<sup>27</sup> Institute of Astronomy and Astrophysics, Academia Sinica, P.O. Box 23-141, Taipei 10617, Taiwan

<sup>28</sup> Institute for Astronomy, ETH Zurich Wolfgang-Pauli-Strasse 27, 8093 Zurich, Switzerland

<sup>29</sup> Astronomical Institute ‘Anton Pannekoek’, University of Amsterdam, Science Park 904, 1098 XH Amsterdam, The Netherlands

<sup>30</sup> Kavli Institute for the Physics and Mathematics of the Universe, The University of Tokyo, Kashiwa 227-8568, Japan

<sup>31</sup> Department of CosmoSciences, Hokkaido University, Sapporo 060-0810, Japan

<sup>32</sup> Astronomical Institute, Tohoku University, Aoba, Sendai 980-8578, Japan

figurations in late 2012 and early 2013 (see Table 1). The receivers were tuned to place  $^{12}\text{CO}$  ( $2 \rightarrow 1$ ) in the upper sideband, although the exact tuning varied slightly between the tracks. The  $^{12}\text{CO}$  ( $2 \rightarrow 1$ ) line was observed with a resolution of 0.2 MHz in the compact and extended configuration, and a resolution of 0.4 MHz in the very extended configuration. All tracks were gain calibrated with 1427-421 and 1325-430 and bandpass calibrated with 3C 279. The absolute flux scale was set by Titan and has a  $\sim 10\%$  uncertainty. The data were calibrated in MIR following standard procedures<sup>33</sup> and then combined and imaged in Miriad (Sault, Teuben, & Wright 1995). The continuum data were concatenated from all chunks with 3.25 MHz resolution, providing  $\sim 7.5$  GHz of continuum bandwidth. The rms in the synthesized beam in the very extended configuration are  $0.35$  mJy beam $^{-1}$  and  $162.5$  mJy km s $^{-1}$  beam $^{-1}$  in the dust continuum and  $^{12}\text{CO}$  ( $2 \rightarrow 1$ ) line emissions, respectively.

The dust continuum image at 1.3 mm and the integrated  $^{12}\text{CO}$  ( $2 \rightarrow 1$ ) line emission map (natural weighting) in the very extended configuration as well as the  $1.6 \mu\text{m}$  polarized intensity image of PDS 70 are shown in Fig. 1. The images of the dust continuum and  $^{12}\text{CO}$  ( $2 \rightarrow 1$ ) emissions in the very extended configuration have a peak flux of  $13.6$  mJy beam $^{-1}$  and  $1.06$  Jy km s $^{-1}$  beam $^{-1}$ , respectively. Meanwhile, in the combined images of the compact; extended; very extended configurations, a total flux of the dust continuum and integrated line emissions above  $3 \sigma$  has  $38.1 \pm 1.1$  mJy and  $3.5 \pm 0.4$  Jy km s $^{-1}$ , respectively. All three images in Fig. 1 show a deficit of flux density in the central regions of the disk, suggesting a central cavity or gap structures in small and large dust grains and the gas. We note that the NIR image alone does not provide convincing proof for the deficit of dust grains in the central region of the disk (Takami et al. 2014). Takami et al. (2014) shows that such a deficit in the NIR flux still allows the possibility of a disk surface that is parallel to the light path from the star, or a disk that is shadowed by structures in the inner radii.

The morphological structures in the dust continuum and NIR polarized intensity are asymmetric:  $1.38 \pm 0.06$  and  $1.32 \pm 0.15$  times brighter in the north-west part of the dust continuum and the south-east part of NIR polarized intensity, respectively, while the brightness of the CO ( $2 \rightarrow 1$ ) map exhibits no clear asymmetries within the limits of observational errors (i.e., it is  $1.43 \pm 0.38$  times brighter in the south-east region). Note that although the orientation of the disk-major axis in the dust continuum image (Fig. 1a) and the NIR polarized intensity image (Fig. 1c) appear different from each other (PA of  $135^\circ$  and  $160^\circ$  respectively), this is due to the elongated beam in the SMA observations.

Fig. 2 shows channel maps of the  $^{12}\text{CO}$  ( $2 \rightarrow 1$ ) line emission with the LSR velocity range from  $2.65$  km s $^{-1}$  to  $8.48$  km s $^{-1}$ . Since the  $^{12}\text{CO}$  line could easily turn out to be optically thick, we can estimate the gas temperature based on the line intensity. The peak flux in the channel maps is  $0.46$  Jy beam $^{-1}$  at  $7.42$  km s $^{-1}$  and suggests  $\sim 28$  K with the Rayleigh-Jeans approximation.

A velocity gradient from the northwest to southeast can be seen in the channel maps (Fig. 2), suggestive of rotation. This velocity gradient can also be seen in the intensity-weighted mean velocity map (Fig. 3a). Assuming PDS 70 is surrounded by the Keplerian disk with an inclination of  $50^\circ$  (Hashimoto et al. 2012), we infer a dynamical mass of the central star with  $0.6$ - $0.8 M_\odot$  in the position-velocity diagram (Fig. 3b), consistent with the value of  $0.82 M_\odot$  estimated by the spectral type of K5 (Riaud et al. 2006). We also found the peak positions between the dust continuum image and the line-emission map are apparently slightly misaligned in Fig. 3(c): the northwest parts are roughly aligned, while the southeast parts have a misalignment with  $\sim 0''.25$  (35 AU). However, the peak-position determination accuracy strongly depends on the peak flux-density and the signal-to-noise ratio; hence, this misalignment seen in our noisy CO data may not be real.

### 3. RADIATIVE TRANSFER MODELING

In our previous studies (Hashimoto et al. 2012; Dong et al. 2012b), we modeled the SED and NIR polarized intensity of PDS 70 using a Monte Carlo radiative transfer (MCRT) code (Whitney et al. 2013) to derive the morphological structure of the dust disk, especially in small dust grains. Whitney’s code follows a two-layer disk model with small (up to  $\sim \mu\text{m}$  size) dust grains in the upper disk-atmosphere and large (up to millimeter size) dust grains in the disk mid-plane (e.g., D’Alessio et al. 2006). Historically, numerical simulations of a disk containing only small dust grains failed to reproduce millimeter-wave emission in typical T Tauri stars due to the low opacity of small dust grains at longer wavelengths (D’Alessio et al. 1999), whereas a disk with only large dust grains was predicted to have no silicate emission bands (D’Alessio et al. 2001) ubiquitously seen in T Tauri stars (e.g., Furlan et al. 2009) due to the gray opacity of large dust grains at shorter wavelengths. Thus, a two-layer disk model has been employed to improve the agreement with observations (e.g., Chiang et al. 2001).

In this paper, we attempt to simultaneously derive the disk properties in small and large dust grains by fitting the SED, the polarized intensity image at NIR, and the dust-continuum image at 1.3 mm using Whitney’s code. Since we mainly focus on the radial distributions of small and large dust grains (especially the radius of the gap) in the modeling efforts, we attempt to derive the gap-radius by comparing radial profiles of synthesized images and observations. Note that the gas is not modeled in this paper.

#### 3.1. Dust Disk Structure and Dust Property

The dust-disk structure assumed in this paper follows that from Hashimoto et al. (2012) and Dong et al. (2012b). We synthesize the SED, the NIR polarized intensity image, and the dust continuum at 1.3 mm utilizing an axisymmetric and flared disk model in which the vertical density structure ( $\rho$  in cylindrical-polar coordinates  $\{R, z\}$ ) in both small and large dust grains is assumed to be Gaussian,

$$\rho(R, z) = \frac{\Sigma(R)}{\sqrt{2\pi}h} \exp\left[-\frac{1}{2}\left(\frac{z}{h}\right)^2\right], \quad (1)$$

<sup>33</sup> <http://cfa-www.harvard.edu/~cqi/mircook.html>

where  $\Sigma$  is a surface density;  $h$  is a scale height varying as a power law with a radius, i.e.,  $h \propto R^p$ . To reduce the number of parameters and simplify, we assume  $p = 1.25^{34}$ , i.e., a mid-plane temperature of  $T \propto R^{-0.5}$  as approximately estimated by millimeter observations (Beckwith et al. 1990). The scale heights of small and large dust grains are generally different, because small dust grains are expected to be coupled well with the gas and might have a similar scale height of the gas whereas large dust grains de-coupled with the gas could be likely to settle in the disk mid-plane due to the stellar gravity. A radial surface density structure ( $\Sigma$ ) in dust grains described in the similarity solution for viscous accretion disks (Lynden-Bell & Pringle 1974; Hartmann et al. 1998) is

$$\Sigma(R) = \Sigma_0 \left( \frac{R}{R_c} \right)^{-q} \exp \left[ - \left( \frac{R}{R_c} \right)^{2-q} \right], \quad (2)$$

where  $\Sigma_0$  is a normalized surface density determined by a total disk mass ( $M_{\text{disk}}$ );  $R_c$  is a characteristic radius;  $q$  is a radial gradient parameter. In Whitney's code, in order to generate a gap structure in a central region of a disk, a surface density of a dust disk inside the gap ( $R_{\text{gap}}$ ) is uniformly scaled down as follows,

$$\Sigma(R) = \delta \Sigma_0 \left( \frac{R}{R_c} \right)^{-q} \exp \left[ - \left( \frac{R}{R_c} \right)^{2-q} \right], \text{ at } R \lesssim R_{\text{gap}}^{(3)}$$

where  $\delta$  is a constant depletion factor. Note that we assume  $q = 1$  as derived in the viscous disk model with  $T \propto R^{-0.5}$  (Hartmann et al. 1998). A radial surface density of small and large dust grains used in our fiducial model is shown in Fig. 4.

Dust properties used in this paper follow Dong et al. (2012b): small dust grains from the standard interstellar-medium dust model (a composition of silicates and graphites; a size distribution of  $n(s) \propto s^{-3.5}$  from  $s_{\text{min}} = 0.0025 \mu\text{m}$  to  $s_{\text{max}} = 0.2 \mu\text{m}$ ) in Kim, Martin, & Hendry (1994) and large dust grains (a composition of carbons and silicates; a size distribution of  $n(s) \propto s^{-3.5}$  from  $s_{\text{min}} = 0.01 \mu\text{m}$  to  $s_{\text{max}} = 1000 \mu\text{m}$ ) from Model 2 in Wood et al. (2002). Opacity ( $\kappa$ ) of small and large dust grains used in our modeling efforts is shown in Fig. 5 (see also Fig. 1 in Dong et al. 2012b).

### 3.2. Results of Modeling Efforts

We have synthesized the NIR polarimetric image, the SED, and the dust continuum of PDS 70 by varying the total mass of the disk ( $M_{\text{disk}}$ ; assuming gas-to-dust mass ratio of 100), mass fraction ( $f$ ) of large dust grains in the total mass of dust grains, scale height ( $h$ ) at 100 AU, depletion factor ( $\delta$ ), size of a gap in large dust grains ( $R_{\text{gap}}^l$ ), and characteristic radius ( $R_c$ ). The size of a gap in small dust grains ( $R_{\text{gap}}^s$ ) is set to 65 AU because NIR imaging constrains this size (Hashimoto et al. 2012; Dong et al. 2012b). Most parameters are similar to those in Hashimoto et al. (2012) and Dong et al. (2012b) except the depletion factor and the characteristic radius.

<sup>34</sup> A scale height is described as  $h \approx c_s \Omega^{-1}$ , where  $\Omega$  is the rotational angular velocity of  $\Omega \propto R^{-1.5}$  in the Kepler rotation;  $c_s$  is the sound speed of  $c_s \propto T^{0.5}$ . If  $T \propto R^{-0.5}$ , then  $h \propto R^{1.25}$ .

Since the procedure in synthesizing NIR polarimetric images in Hashimoto et al. (2012) and Dong et al. (2012b) did not subtract a 'polarized halo (described in § 2.1 in Hashimoto et al. 2012)', the depletion factor and the characteristic radius in our fiducial models are slightly different from our previous studies. To simplify, we assume the depletion factor and the characteristic radius between small and large dust grains are same. In addition, the scale height inside and outside the gap is also the same. The parameters in the fiducial model and previous model are shown in Table 2.

Fig. 6 shows the difference of synthesized NIR images between the fiducial model and the previous model. The SEDs in two models (Fig. 6d) are consistent, whereas the radial profiles along the major axis are slightly different (Fig. 6e). After modeling, we subtracted the polarized halo from two synthesized images using IRAF<sup>35</sup> as a same manner in Hashimoto et al. (2012). We also added an offset value of 0.14 mJy arcsec<sup>-2</sup> to the synthesized NIR images. Since polarized intensity (PI) is calculated as square-root of sum of squares in stokes  $Q$  and  $U$ , i.e.,  $PI = \sqrt{Q^2 + U^2}$ , the noise becomes always positive. The value of 0.14 mJy arcsec<sup>-2</sup> is the averaged noise level in our NIR observations. These two operations, subtracting the polarized halo and adding the offset value of averaged noise, result in the difference of radial profiles of two models.

As a result of our MCRT modeling with  $9 \times 10^8$  photons, we found the apparent size of the gap is different (Fig. 7): 80 and 65 AU in a radius in large and small dust grains, respectively. We also show the dust continuum images with fiducial parameters in Table 2 with different sizes of a gap in large dust grains ( $R_{\text{gap}}^l = 65, 80, \text{ and } 95 \text{ AU}$ ) in Fig. 7. Dust continuum images are convolved with a 2D elliptical Gaussian function of  $0''.97 \times 0''.48$  at PA = 12.33° which is a beam-size in our SMA observations. The synthesized dust continuum with a gap-radius of 80 AU (Fig. 7b) is matched well with SMA observations except for the asymmetries due to axisymmetric structures assumed in our modeling efforts. We compare the averaged radial profile of the observed dust continuum with that of synthesized dust continuum (Fig. 7d). The radial profiles along the apparent major-axis at PA of 135° are averaged in the northwest and southeast parts. Though the shapes of the profiles are reproduced well with the synthesized dust continuum with a gap-radius of 80 AU, the flux density of the synthesized dust continuum needs to be multiplied by 1.155 in order to obtain the consistent absolute flux density. This result, that the radial profile of the observations is brighter than those of the synthesized dust continuum, implies the flux density may be gathered in the northwest rather than azimuthally symmetric.

The synthesized SEDs in Fig. 7(e) do not differ significantly except around 200  $\mu\text{m}$ . Large dust grains in the disk-midplane are heated by the emission from the upper layer of the disk (c.f., Fig. 1 in D'Alessio et al. 2006). Since the temperature of the upper layer of the disk generally decreases with the distance from a central

<sup>35</sup> IRAF is distributed by the National Optical Astronomy Observatories, which are operated by the Association of Universities for Research in Astronomy, Inc., under cooperative agreement with the National Science Foundation.

star, the disk-midplane irradiated by the upper layer also cools down with the radius. The different gap-radius in large dust grains would reflect the amount of thermal emission around  $200 \mu\text{m}$  in the SED. The three synthesized NIR polarimetric images are reasonably consistent with each other (Fig. 7f). Since the opacity at NIR wavelengths in small dust grains is  $\sim 10$  times larger than that in large dust grains (Fig. 5); and the disk in large dust grains is located in the midplane, minor geometric differences of the disk in large dust grains do not affect the NIR scattering image.

Our modeling efforts in this paper are relatively simple, and the above fiducial model would not be the best solution. Even so, our disk model with a gap consistently explains the the observed images at NIR and millimeter wavelengths and the SEDs. In particular, our modeling suggests different gap radii for small and large grains. Further complicated disk models (e.g., not sharp gap-edge) and fitting the visibility profile of the dust continuum will be presented elsewhere.

#### 4. DISCUSSION

We discuss scenarios to account for the observational features of PDS 70, especially the asymmetries and the different gap-radii. Before discussing the possible origin of the complicated disk around PDS 70, we summarize six main observational properties of PDS 70.

- (a) Infrared to millimeter observations and our modeling suggest that the depletion of the gas in the disk as well as large and small dust grains within tens of AU in radius (§ 2 and 3.2).
- (b) The contrast ratio in the dust continuum of 1.4 (§ 2).
- (c) The above model suggests different gap-radii in small and large dust grains, 65 and 80 AU, respectively (§ 3.2).
- (d) The existence of the optically thick inner disk of small dust grains at  $\sim 0.1$  AU (Hashimoto et al. 2012).
- (e) The upper limit of a planetary mass in the gap is estimated to be  $\sim 2 M_{\text{Jup}}$  in our previous studies (Hashimoto et al. 2012) based on a hot-start planet model (Baraffe et al. 2003) and the lack of detection of any point sources in the image.
- (f) The low mass accretion; PDS 70 is a weak-lined T Tauri star (a  $\text{H}\alpha$  equivalent width of  $2.0 \text{ \AA}$ ; Gregorio-Hetem & Hetem 2002)

Thereby, scenarios proposed to explain both the asymmetries and the different gap-radii of PDS 70 should also explain all above observational constraints. In this section, we firstly discuss the possible origin of the asymmetries, and then, different gap-sizes independently. Finally, we discuss the possible scenario responsible for all observational features and suggest how to further constrain a proposed scenario in future observations.

#### 4.1. Azimuthal Asymmetry

Fig. 1 show an asymmetric brightness in the dust continuum at 1.3 mm and NIR polarized intensity. Such asymmetries in the dust continuum have been detected in other transitional disks, e.g., LkH $\alpha$  330 (Brown et al. 2008) and SAO 206462 (Brown et al. 2009). The contrast ratio of the peak-emission to the opposite-side of the disk is likely to be higher among transitional disks around intermediate mass stars (e.g.,  $\sim 30$  in HD 142527; Casassus et al. 2013; Fukagawa et al. 2013 and  $\sim 130$  in WLY 2-48; van der Marel et al. 2013) than among solar-mass stars (e.g.,  $\sim 1.1$ - $1.2$  in UX Tau A, DoAr 44, and LkCa 15; Andrews et al. 2011). PDS 70's contrast ratio of 1.4 is similar to 1.3-1.5 in SAO 206462 (Brown et al. 2009; Pérez et al. 2014) and slightly higher than that among solar-mass stars. The physical interpretation of the asymmetries is still under debate: gravitational interaction between planet and disk (e.g., Kley & Nelson 2012), large anticyclonic vortex induced by the Rossby wave instability (e.g., Regály et al. 2012), eccentric disk formed by a massive planet (e.g., Kley & Dirksen 2006), and an azimuthal variance of temperature and opacity. In this sub-section, we discuss the potential origin of asymmetric features observed in PDS 70.

*Disk-planet interaction* — An embedded massive planet with a mass of  $\gtrsim 1 M_{\text{Jup}}$  could open a gap and excite a spiral density wave in the disk due to tidal interactions, while a less massive planet could only excite a wake because the perturbation is not strong enough (see Papaloizou et al. 2007; Kley & Nelson 2012 for a review). These interactions could also lead to exchange of angular momentum of the gas and dust grains in the disk, and are expected to result in asymmetric structures in the disk as well. Actually, previous studies have demonstrated the asymmetries in the surface density of the disk using hydrodynamic simulations (Dodson-Robinson & Salyk 2011; Isella et al. 2013). Though the relationship between disk-planet interaction and asymmetric structures in the disk still remains to be intensively investigated, a single massive planet could tend to induce azimuthally symmetric structures except spirals (Kley & Nelson 2012), whereas multiple massive planets could create azimuthal asymmetries (Dodson-Robinson & Salyk 2011; Isella et al. 2013). Hence, the existence of multiple planets would be one of the key points to explain the observed asymmetries in PDS 70. The possible existence of (unseen) multiple planets opening the gap around PDS 70 has already been argued in Hashimoto et al. (2012); Dong et al. (2012b) and been supported by following two aspects: the large gas-gap around PDS 70 with a radius of  $\sim 65$  AU (Fig. 1c) could be explained by only multiple planets (Zhu et al. 2011; Dodson-Robinson & Salyk 2011); a gap structure (optically thick inner and outer disks separated by an optically thin region) inferred from NIR imaging (Fig. 1c) and the SED (Fig. 7e) is most like due to disk-planet interaction rather than other inside-out scenarios (grain growth; photoevaporation; see § 1). Furthermore, Hashimoto et al. (2012) put an upper limit of the planetary mass of only  $\sim 2 M_{\text{Jup}}$  in the gap based on  $L'$  band ( $3.8 \mu\text{m}$ ) imaging, thus being unable to discard the existence of unseen massive planets with a mass of  $\sim 1 M_{\text{Jup}}$ . Therefore, though further quantitative comparisons be-

tween observations and numerical simulations (e.g., comparisons between the observed PDS 70’s contrast ratio of 1.4 and simulations) are still necessary, we anticipate the observed asymmetries in the disk of PDS 70 might be induced by interactions between unseen multiple planets and the disk.

*Anticyclonic vortex* — Asymmetric structures in a disk can be explained without any planets. In the last decade, several transitional disks show asymmetric dust continuum emission (Piétu et al. 2005; Brown et al. 2009; Andrews et al. 2011; Pérez et al. 2014) and has been explained with large anticyclonic vortex potentially formed by the Rossby wave instability (RWI; Lovelace et al. 1999; Regály et al. 2012). RWI is excited at steep gas-pressure gradients in an overdense region where is thought to be an outer edge of the ‘dead zone’ (Gammie 1996). The gas in the disk is generally transported from the outer disk through mass accretion, possibly triggered by the magnetorotational instability (MRI; Balbus & Hawley 1991). MRI becomes active when the ionization state of the gas is sufficient, meaning an ionized upper layer of a disk and a less dense outer-disk are prone to induce MRI. Conversely, a dense region in the disk-midplane would have less effective ionization because of gas self-shielding against ionization radiation, resulting in a dead zone where mass accretion by MRI is strongly reduced. As a result, a gas-overdense region is expected to form at the boundaries of the dead zone (Varnière & Tagger 2006; Terquem 2008), leading RWI to launch anticyclonic vortices. The radius of the outer edge in the dead zone strongly depends on the amount of dust grains (Sano et al. 2000) because degrees of ionization in the gas are suppressed by recombination of ions and electrons at grain surfaces. Assuming the minimum-mass solar nebula (Hayashi, Nakazawa, & Nakagawa 1985), Sano et al. (2000) estimated the dead zone’s outer edge is about 20 AU in radius. Since this radius is also a function of the disk’s properties (e.g., a vertical magnetic field, density, and a temperature of a disk; Okuzumi & Hirose 2011), anticyclonic vortices might take place at a radius of 80 AU in the case of PDS 70. However, this scenario would not explain the gap structure even if it explains asymmetric structures; hence it is unlikely that an anticyclonic vortex induced at the outer-edge of the dead zone could be the main scenario.

Steep gas-pressure gradients can also form at the gap-edge sculpted by massive planets (Papaloizou et al. 2007; Kley & Nelson 2012), resulting in anticyclonic vortices (e.g., Li, Li, & Koller 2005; Lin & Papaloizou 2010; Zhu et al. 2014; Zhu & Stone 2014). Coriolis force in a vortex effectively leads large dust grains into the central vortex (e.g., Fig. 1 in Barge & Sommeria 1995), resulting in an increase in the surface density of the large dust grains by more than a factor of 10-100 for fastest drifting particles (Zhu et al. 2014; Zhu & Stone 2014). van der Marel et al. (2013) modeled the asymmetric structures in the dust continuum around WLY 2-48, which has the large contrast ratio of 130, with a vortex-shaped dust trap triggered by a companion. Although PDS 70 has a contrast ratio in flux density of only 1.4, this value may be due to the convolution of the large beam size ( $\sim 1''$ ) in our observations. Thus this scenario of the vortex at the planet-induced gap-edges

would be applied to explain not only the large contrast ratio in HD 142527 and WLY 2-48 with  $\sim 30$  and  $\sim 130$ , respectively, but also the case of PDS 70.

*Variance of Temperature and Opacity* — When a disk is optically thin, the observed azimuthal flux density  $F_\nu$  is

$$F_\nu \approx \kappa_\nu \times M_d \times B_\nu(T_d) \times d^{-2}, \quad (4)$$

where  $\kappa_\nu$  and  $T_d$  are the opacity and temperature of a disk with a mass of  $M_d$ ,  $B_\nu$  is the blackbody intensity, and  $d$  is the distance (c.f., Draine 2006). Since the Rayleigh-Jeans limit ( $h\nu \ll kT_d$ ) can be applied at (sub-)millimeter wavelengths (Beckwith et al. 1990; Beckwith & Sargent 1991),  $F_\nu$  is

$$F_\nu \propto \nu^2 \times \kappa_\nu \times M_d \times T_d. \quad (5)$$

Hence, assuming the azimuthally-symmetric dust opacity  $\kappa_\nu$  and mass-distributions of the dust grains, azimuthal distributions of the observed flux density depend on disk temperature. As mentioned in § 3.2, since the disk-midplane is heated by the emission from the upper layer of the disk, if the stellar radiation is interrupted by an asymmetric inner disk (e.g., a warp; an asymmetric puff-up), a shadow cast from the inner disk might cool down disk temperature in the outer disk. Disk temperature of large dust grains in the mid-plane around  $r = 80$  AU of PDS 70 simulated in our modeling efforts is 23 K, corresponding to the azimuthal temperature variance of 16-23 K using the contrast ratio of the flux density in PDS 70 with 1.4. Thus, we cannot rule out this scenario based on our observations. Though whether this scenario of shadowing can directly affect on (sub-)millimeter radiation and azimuthal redistribution in a (closer to) optically thin environment is still ambiguous, monitoring observations would be useful to test the shadowing-scenario, because a shadow cast from the inner disk is co-rotating with the inner disk. The Keplerian orbital velocity ( $\omega$ ) of the inner disk at 0.1 AU (where is optically thick in Fig. 4) is given by

$$\omega \approx 27 \left( \frac{M}{0.8 M_\odot} \right)^{\frac{1}{2}} \left( \frac{r_d}{0.1 \text{ AU}} \right)^{-\frac{3}{2}} [\text{deg day}^{-1}], \quad (6)$$

where  $M$  is the mass of the central star and  $r_d$  is the orbital radius of the inner disk. Such rotation could be observed within a few months. Furthermore, a non-axisymmetric illumination from the central star (Takami et al. 2014) possibly causes asymmetric distributions of the disk temperature. Assuming PDS 70 has the rotational velocity of  $\sim 10 \text{ km s}^{-1}$  and a radius of  $1.39 R_\odot$  (Gregorio-Hetem & Hetem 2002), the rotation period is  $\sim 50$  days. Such a periodic fluctuation could be also observable within a few months.

Note that though above discussions are based on the azimuthally-symmetric dust opacity, asymmetrically distributed dust opacity could also affect the flux density. If the dust opacity  $\kappa_\nu$  is assumed to have a power-law dependence on frequency,  $\kappa_\nu \propto \nu^\beta$  (Beckwith et al. 1990; Beckwith & Sargent 1991), the observed azimuthal flux density in equation (5) becomes  $F_\nu \propto \nu^\alpha$  (where  $\alpha = \beta + 2$ ) assuming azimuthally-symmetric disk temperature and mass distributions of the dust grains. A power-law index  $\beta$  is known to strongly depend on size distributions

and maximum sizes of dust grains (Draine 2006). For instance, interstellar medium (ISM) dust mainly consisting of sub- $\mu\text{m}$  size grains which are less (sub-)millimeter emitters shows  $\beta \approx 1.7$  (e.g., Li & Draine 2001), while circumstellar disks consisting of both small and large dust grains show  $\beta \sim 0$  (e.g., Andrews & Williams 2007). Thus, if grain growth locally takes place in the disk due to, for example, anticyclonic vortices, asymmetric dust continuum emission could be observed. The parameter  $\beta$  in  $\kappa_\nu$  of large dust grains in our modeling is  $\sim 0.6$  (Fig. 5), and  $\beta$  changing with  $\delta\beta \sim 0.017$  reproduces the contrast ratio of 1.4 of PDS 70 at 1.3 mm. When dust grains grow into larger dust grains in the disk, this change in  $\beta$  would be reasonable. Hence, though we cannot exclude this scenario based on our single-wavelength observations, future high-resolution multi-color radio interferometric observations with ALMA could reveal azimuthal  $\beta$  distributions, allowing the investigation of whether dust grains locally evolve in the disk.

*Eccentricity* — Numerical calculations expect that when a massive planet with a stellar-to-planet mass ratio of  $q \gtrsim 3\text{--}5 \times 10^{-3}$  is embedded in the disk, an eccentric disk can form at the gap-edge (eccentricity of up to  $\sim 0.25$ ; Kley & Dirksen 2006; Ataiee et al. 2013; Regály, Király, & Kiss 2014). Keplerian orbital velocity at the apocenter of the elliptic orbits is slower than at the pericenter, resulting in a possible enhancement of disk materials at the apocenter of the disk. This scenario makes a ‘traffic jam’ instead of a dust-trap, suggesting a lower azimuthal contrast than that in the vortex. According to Ataiee et al. (2013), the contrast ratio of the disk mass between the apocenter and the pericenter is  $\sim 1.5$  (see Fig. 3 in Ataiee et al. 2013). This value is consistent with that of PDS 70. However, the necessary minimum-planetary-mass to induce an eccentric disk around PDS 70 would be  $\sim 2\text{--}4 M_{\text{Jup}}$ ; such planetary-mass objects in the gap should be detected in our previous observations (see Fig. 2f in Hashimoto et al. 2012). One of the differences in this scenario compared to the above is that the asymmetries in an eccentric disk are fixed at the same position instead of co-moving with planets or vortices; hence future follow-up observations could confirm whether an eccentric disk forms around PDS 70.

#### 4.2. Different Radial Structures in Dust Grains

Our observations and modelling efforts suggest that the disk around PDS 70 has different radial structures in large and small dust grains: a gap of  $r = 80$  AU for large dust grains and 65 AU for small dust grains (§ 3.2; Fig. 7). In § 1, we mentioned grain growth and photoevaporation as potential scenarios to explain the properties of transitional disks (e.g., Clarke, Gendrin, & Sotomayor 2001; Dullemond & Dominik 2005). As discussed by other authors (e.g., Espaillat et al. 2014), these two scenarios are expected to result in inside-out disk-dispersal. Since PDS 70 has an optically thick inner disk at  $\sim 0.1$  AU (Fig. 4; Hashimoto et al. 2012), these two would be less dominant in PDS 70. Another possible scenario is disk-planet interaction (e.g., Kley & Nelson 2012). However, *only* gravitational interaction between the disk and planet might result in similar radial structures in three disk components (the gas and the large and small dust

grains), i.e., no radial difference; thus *only* disk-planet interaction would also be less likely in PDS 70. Other scenarios mentioned in § 1 (dust filtration and radiation pressure) need planet(s) in the gap. In this sub-section, we briefly review and discuss the combinations of scenarios: disk-planet interaction with dust filtration and/or radiation pressure.

Dust filtration (Rice et al. 2006; Zhu et al. 2012; Pinilla, Benisty, & Birnstiel 2012; de Juan Ovelar et al. 2013; Owen 2014) is induced at the outer edge of the gap. Dust filtration has been originally suggested to explain apparently contradictory transitional disk properties: a T-Tauri-star-like moderate mass accretion rate ( $\dot{M} \sim 10^{-8}$  to  $10^{-9} M_\odot \text{ yr}^{-1}$ ; Najita, Strom, & Muzerolle 2007) with an optically thin or empty inner hole. Since the disk-materials in the inner disk are resupplied from the outer disk through mass accretion, moderate mass accretion and an inner hole are apparently inconsistent. To interpret these transitional disk properties, theorists make use of a physical consequence that dust particles are trapped at gas-pressure maxima. When a dust particle embeds in a gaseous disk where the pressure has a radially negative gradient, since the gas rotates with the sub-Keplerian velocity, a dust particle feels a headwind and loses angular momentum. On the other hand, when a gaseous disk’s pressure has a radially positive gradient, for example, at the outer edge of the gap, since the gas rotates with the super-Keplerian velocity, a dust particle feels a tailwind and gains angular momentum. Eventually, dust particles are led into gas-pressure maxima. The gas can still accrete onto the central star through the gap (Lubow & D’Angelo 2006) even there are multiple planets in the gap (Dodson-Robinson & Salyk 2011; Zhu et al. 2011). That is how large dust grains are distributed at gas-pressure maxima, whereas moderate mass accretion is still observable.

Zhu et al. (2012) demonstrated that though dust filtration with a single or multiple planets affects (sub-)millimeter dust particles, which possibly accounts for (sub-)millimeter observations of large gapped ( $r \gtrsim 20$  AU) transitional disks with moderate mass accretion of  $\gtrsim 10^{-8}$  to  $10^{-9} M_\odot \text{ yr}^{-1}$ , the filtration process hardly affects (sub-)micron sized dust particles since small dust grains are generally coupled well with the gas. This can nicely explain the missing gaps in NIR scattered light images of some transitional disks (Dong et al. 2012a), such as SR 21 (Follette et al. 2013), SAO 206462 (Muto et al. 2012), and MWC 758 (Grady et al. 2013). Subsequent studies in dust filtration (Pinilla, Benisty, & Birnstiel 2012) calculated the position of gas pressure maxima depends on disk viscosity, the planetary mass, and location (e.g., a gas pressure maximum at 30 and 50 AU when 1 and 9  $M_{\text{Jup}}$  at 20 AU, respectively, in Fig. 1 in Pinilla, Benisty, & Birnstiel 2012); de Juan Ovelar et al. (2013) showed observed radii of the gap in the NIR and sub-millimeter wavelengths could also depend on the planetary mass and location (e.g., gap radii in the NIR and sub-millimeter wavelengths are 20 and 30 AU, respectively, when a planet with 1  $M_{\text{Jup}}$  at 20 AU in Fig. 2 in de Juan Ovelar et al. 2013). The radius of the gap in the NIR wavelengths could reflect the scattered po-

sition at the outer gap-edge of the disk in small dust grains carved by a planetary perturbation, while the radius in the (sub)-millimeter wavelength reflects the peak position of the dust surface-density (i.e., gas pressure-maximum which slightly locates at the far side; see Fig. 7 in de Juan Ovelar et al. 2013). The dependence of the dust-gas coupling on the size of the dust grains leads to different gap-radii at different wavelength, as seen in PDS 70. Such disk systems have been reported in SAO 206462 (Garufi et al. 2013; Pérez et al. 2014), HD 100546 (Avenhaus et al. 2014; Pineda et al. 2014), and Sz 91 (Tsukagoshi et al. 2014); thus PDS 70 is not unique.

As pointed out by Zhu et al. (2012), one problem in dust filtration is that it is difficult to account for the low NIR excess generally seen in transitional disks. In addition to dust filtration, to reduce the NIR excess generated from small dust grains, ‘a planetary accretion luminosity’ was proposed by Owen (2014) in which small dust grains are expected to push back by radiation pressure from an accreting planet, resulting in allowing the dust-free gas to accrete onto the central star (Owen 2014). This scenario would be useful to explain the properties of general transitional disks with the reduced NIR excess and moderate mass accretion. However, in contrast to general transitional disks, weak-line T Tauri star PDS 70 should have low mass accretion (a  $H\alpha$  equivalent width of  $2.0 \text{ \AA}$ ; Gregorio-Hetem & Hetem 2002).

#### 4.3. Possible Origin of Complicated Disk-Structures

Though we have discussed the possible scenarios to explain the asymmetries in PDS 70, all proposed scenarios except eccentricity are hardly excluded based on our single epoch and single wavelength observations with SMA (§ 4.1). On the other hand, we found disk-planet interaction + dust filtration could account for different radial structures in small and large grains (§ 4.2). In this sub-section, we discuss whether disk-planet interaction + dust filtration is potentially responsible for the complicated structures of the disk around PDS 70.

Planet(s) in the gap could reduce mass accretion and might explain the low mass accretion of PDS 70. Though mass accretion onto a planet is not conclusively understood, in general, a more massive planet (e.g.,  $10 M_{\text{Jup}}$ ) or multiple planets (e.g.,  $1 M_{\text{Jup}}$ ) could reduce mass accretion onto the central star. Since the existence of such a single  $10 M_{\text{Jup}}$  planet was already ruled out in our previous studies (Hashimoto et al. 2012), accreting multiple planets remain as a possible scenario. If a single planet with  $\sim 1 M_{\text{Jup}}$  can be assumed to have sufficient mass accretion onto the planet itself and induce dust filtration, this planet might be responsible for the large-gapped disk-structure in the dust continuum (Pinilla, Benisty, & Birnstiel 2012) and low accretion rate of PDS 70. However, a single planet would likely induce a relatively symmetric structure in the disk (Kley & Nelson 2012) and thus be inconsistent with the asymmetries observed in PDS 70. Meanwhile, a single planet with  $\sim 1 M_{\text{Jup}}$  could create the asymmetries in the disk if vortices take place at the gap-edge sculpted by this single planet. However, a single planet is expected to create a narrow gap in the gas and small dust grains (i.e.,  $r \lesssim 15 \text{ AU}$ ; Zhu et al. 2011; Dodson-Robinson & Salyk 2011); hence a single accreting planet inducing vortices

would be ruled out as the origin of the large NIR gap around PDS 70. Remaining accreting multiple planets could explain both of low mass accretion and the asymmetries of the large gapped-disk in PDS 70. These combinations could also induce dust filtration at the gap-edge and are likely to account for the different gap-radii in the NIR and millimeter wavelengths.

To summarize, accreting multiple planets inducing dust filtration at the outer gap-edge could explain all observed properties of PDS 70: different observed radii of the gap in the different wavelengths; low mass accretion onto the central star; a depletion of disk components inside the gap except the optically thin inner disk; no very massive planets in the gap. However, direct observational evidence of dust filtration has not been detected in any disk system. One conclusive observational proof of dust filtration would be ‘a gap in the gas’ (see, e.g., Fig. 7 in de Juan Ovelar et al. 2013). As mentioned, in the outside of the planetary orbit, a combination of positive and negative gas-pressure gradients is critical to trap large dust grains at gas-pressure maxima. Inside the planetary orbit, gas-pressure would have only negative gradients, resulting in the depletion of large dust grains. Future ALMA observations with high-resolution and high-sensitivity will enable the detection of a gas gap. Furthermore, detecting any planets in the gap would be important to verify whether planets form gap structures in the dust grains and induce dust filtration. A hint to enhance the detectability of planets in the optical/NIR wavelength may be the planetary accretion luminosity (Owen 2014). Though a low-mass binary, a companion in the gap of HD 142527 (a mass of  $2.2 M_{\odot}$ ; a distance of  $145 \text{ pc}$ ; an age of  $5 \text{ Myr}$ ; Verhoeff et al. 2011) exhibit an accretion luminosity and was detected in the narrow band of  $H\alpha$  (Close et al. 2014). Therefore, integral field spectroscopy combined with angular differential imaging (ADI; Marois et al. 2006) or spectral differential image (SDI; Racine et al. 1999) with ADI focusing on accretion-sensitive lines such as  $H\alpha$  ( $0.656 \mu\text{m}$ );  $\text{Pa}\beta$  ( $1.282 \mu\text{m}$ );  $\text{Br}\gamma$  ( $2.166 \mu\text{m}$ );  $\text{H}_2 v=1-0 \text{ S}(1)$  ( $2.122 \mu\text{m}$ ) may increase the detectability and allow discovery of accreting planets in the gap.

## 5. CONCLUSION

We present the dust continuum at  $1.3 \text{ mm}$  and  $^{12}\text{CO } J = 2 \rightarrow 1$  line emission of the pre-transitional disk around PDS 70 obtained with SMA, and compare these with NIR ( $1.6 \mu\text{m}$ ) polarized intensity image from our previous studies to investigate the radial distributions of the gas and the large (millimeter size) and small ( $\mu\text{m}$  size) dust grains in the disk. The main observational results are as follows.

- Three disk-components (the gas and the large and small dust grains) show the deficit of flux density in the central region of the disk, suggesting depletion of the materials except small dust grains. High-resolution observations using ALMA would give more stringent constraints on the gas and large dust grains in the inner disk.
- Both large and small dust grains show azimuthal asymmetries. The contrast ratio of the flux density at the peak position to that at the opposite



side is 1.4 in the dust continuum. Since other transitional disks around solar-mass stars have the contrast ratio is  $\sim 1.1$ -1.2, the PDS 70's contrast ratio is slightly higher among solar-mass stars.

- The results of Monte Carlo radiative transfer models suggest different radii for the gap edges: 80 and 65 AU for large and small grains, respectively.
- We observed a velocity gradient from the northwest to southeast in  $^{12}\text{CO } J = 2 \rightarrow 1$  line emission, suggesting a rotating disk around PDS 70. The position-velocity diagram of the CO gas infers the dynamical mass of PDS 70 of 0.6-0.8  $M_{\odot}$ , which is consistent with the spectral type of K5.

We have discussed the possible origin of the azimuthal asymmetries in the disk. Though definite conclusions are not reached from our SMA and previous Subaru observations, we anticipate gravitational interaction between multiple planets and the disk, or azimuthal temperature and opacity variance, or anticyclonic vortex could be responsible for the observed asymmetries. Future follow-up observations to test opacity distributions and azimuthal rotations of the asymmetries are expected to put further constraints.

Finally, gap formation with different gap-radii in large and small grains around PDS 70 have also been dis-

cussed. As discussed in Hashimoto et al. (2012) and Dong et al. (2012b), both grain growth and photoevaporation are unlikely because they require an inside-out process that directly contradicts the presence of optically thick inner disk around PDS 70. We argue that combinations of accreting multiple planets and dust filtration explain the observations of the gap structure, low mass accretion, and different radii in the outer gap-edge as well as the asymmetries of PDS 70. Future observations to confirm the existence of multiple planets and dust filtration are desirable. In ALMA cycle 2, a spatial resolution will be comparable to 0."1-0."2 of NIR observations. Such a higher spatial resolution could resolve local density-enhancement possibly due to anticyclonic vortices at the gap-edge; thus our understanding of complicated disk-structures around PDS 70 will be improved in the near future.

We are grateful to an anonymous referee for providing useful comments leading to an improved paper. We appreciate support from the SMA staff. This work is partly supported by a Grant-in-Aid for Science Research in a Priority Area from MEXT Japan, by the Mitsubishi Foundation, and by the U.S. National Science Foundation under Awards No. 1009203 and 1009314. This work is partially supported by Grant-in-Aid for JSPS Fellows (No. 25-8826).

#### REFERENCES

- Alexander, R. D., Clarke, C. J., & Pringle, J. E. 2006, *MNRAS*, 369, 229
- Alexander, R. D. & Armitage, P. J. 2007, *MNRAS*, 375, 500
- Andrews, S. M. & Williams, J. P. 2007, *ApJ*, 671, 1800
- Andrews, S. M., Wilner, D. J., & Espaillat, C. et al. 2011, *ApJ*, 732, 42
- Ataiee, S., Pinilla, P., & Zsom, A. et al. 2013, *A&A*, 553, L3
- Avenhaus, H., Quanz, S. P., & Meyer, M. R. et al. 2014, *ApJ*, 790, 56
- Balbus, S. A. & Hawley, J. F. 1991, *ApJ*, 376, 214
- Baraffe, I. Chabrier, G., Barman, T. S., Allard, F., & Hauschildt, P. H. 2003, *A&A*, 402, 701
- Barge, P. & Sommeria, J. 1995, *A&A*, 295, L1
- Beckwith, S. V. W., Sargent, A. I., Chini, R. S., & Guesten, R. 1990, *AJ*, 99, 924
- Beckwith, S. V. W. & Sargent, A. I. 1991, *ApJ*, 381, 250
- Birnstiel, T., Andrews, S. M., & Ercolano, B. 2012, *A&A*, 544, 79
- Brown, J. M., Blake, G. A., Qi, C., Dullemond, C. P., & Wilner, D. J. 2008, *ApJ*, 675, L109
- Brown, J. M., Blake, G. A., & Qi, C. et al. 2009, *ApJ*, 704, 496
- Brown, J. M., Herczeg, G. J., Pontoppidan, K. M., & van Dishoeck, E. F. 2012, *ApJ*, 744, 116
- Bruderer, S., van der Marel, N., van Dishoeck, E. F., & van Kempen, T. A. 2014, *A&A*, 562, A26
- Calvet, N., D'Alessio, P., & Watson, D. M. et al. 2005, *ApJ*, 630, L185
- Casassus, S., van der Plas, G. M., & Perez, S. et al. 2013, *Nature*, 493, 191
- Chiang, E. I., Joungh, M. K., & Creech-Eakman, M. J. et al. 2001, *ApJ*, 547, 1077
- Clarke, C., Gendrin, A., & Sotomayor, M. 2001, *MNRAS*, 328, 485
- Close, L. M., Follette, K. B., & Males, J. R., et al. 2014, *ApJ*, 781, L30
- Cutri, R. M., et al. 2013, Explanatory Supplement to the allWISE Data Release Products, Tech. rep
- D'Alessio, P., Calvet, N., Hartmann, L., Lizano, S., & Cantó, J. 1999, *ApJ*, 527, 893
- D'Alessio, P., Calvet, N., & Hartmann, L. 2001, *ApJ*, 553, 321
- D'Alessio, P., Calvet, N., Hartmann, L., Franco-Hernández, R., & Servín, H. 2006, *ApJ*, 638, 314
- Debes, J. H., Jang-Condell, H., Weinberger, A. J., Roberge, A., & Schneider, G. 2013, *ApJ*, 771, 45
- Dodson-Robinson, S. & Salyk, C. 2011, *ApJ*, 738, 131
- Dong, R., Rafikov, R., & Zhu, Z. et al. 2012, *ApJ*, 750, 161
- Dong, R., Hashimoto, J., & Rafikov, R. et al. 2012, *ApJ*, 760, 111
- Draine, B. T. 2006, *ApJ*, 636, 1114
- de Juan Ovelar, M., Min, M., Dominik, C., et al. 2013, *A&A*, 560, A111
- Dullemond, C. P. & Dominik, C. 2005, *A&A*, 434, 971
- Espaillat, C., Muzerolle, J., Najita, J., et al. 2014, in *Protostars and Planets VI*, in press
- Follette, K. B., Tamura, M., & Hashimoto, J. et al. 2013, *ApJ*, 767, 10
- Fukagawa, M., Tamura, M., Itoh, Y., Kudo, T., Imaeda, Y., Oasa, Y., Hayashi, S. S., & Hayashi, M. 2006, *ApJ*, 636, L153
- Fukagawa, M., Tsukagoshi, T., & Momose, M. et al. 2013, *PASJ*, 65, L14
- Furlan, E., Watson, D. M., & McClure, M. K. et al. 2009, *ApJ*, 703, 1964
- Gammie, C. F. 1996, *ApJ*, 457, 355
- Garufi, A., Quanz, S. P., & Avenhaus, H. et al. 2013, *A&A*, 560, A105
- Geers, V. C., Pontoppidan, K. M., & van Dishoeck, E. F. et al. 2007, *A&A*, 469, L35
- Grady, C. A., Muto, T., & Hashimoto, J. et al. 2013, *ApJ*, 762, 48
- Gregorio-Hetem, J., & Hetem, A. 2002, *MNRAS*, 336, 197
- Hartmann, L., Calvet, N., Gullbring, E., & D'Alessio, P. 1998, *ApJ*, 495, 385
- Hashimoto, J., Tamura, M., & Muto, T. et al. 2011, *ApJ*, 729, L17
- Hashimoto, J., Dong, R., & Kudo, T. et al. 2012, *ApJ*, 758, L19
- Hayashi, C., Nakazawa, K., & Nakagawa, Y. 1985, in *Protostars and Planets II*, ed. D. C. Black, & M. S. Matthews (Tucson, AZ: Univ. Arizona Press), 1100
- Isella, A., Pérez, L. M., & Carpenter, J. M. et al. 2013, *ApJ*, 775, 30
- Kim, S.-H., Martin, P. G., & Hendry, P. D. 1994, *ApJ*, 422, 164
- Kley, W. & Dirksen, G. 2006, *A&A*, 447, 369
- Kley, W. & Nelson, R. P. 2012, *ARA&A*, 50, 211
- Li, A. & Draine, B. T. 2001, *ApJ*, 554, 778
- Li, H., Li, S., & Koller, J. et al. 2005, *ApJ*, 624, 1003
- Lin, M.-K. & Papaloizou, J. C. B. 2010, *MNRAS*, 405, 1473
- Lovelace, R. V. E., Li, H., Colgate, S. A., & Nelson, A. F. 1999, *ApJ*, 513, 805
- Lubow, S. H. & D'Angelo, G. 2006, *ApJ*, 641, L526
- Lynden-Bell, D. & Pringle, J. E. 1974, *MNRAS*, 168, 603
- Lyo, A. -R., Ohashi, N., Qi, C., Wilner, D. J., & Su, Y. -N. 2011, *AJ*, 142, 151
- Marois, C., Lafrenière, D., Doyon, R., Macintosh, B., & Nadeau, D. 2006, *ApJ*, 641, 556
- Mathews, G. S., Williams, J. P., & Ménard, F. 2012, *ApJ*, 753, 59
- Mayama, S., Hashimoto, J., & Muto, T. et al. 2012, *ApJ*, 760, L26

- Muto, T., Grady, C. A., & Hashimoto, J. et al. 2012, *ApJ*, 748, L22
- Najita, J. R., Strom, S. E., & Muzerolle, J. 2007, *MNRAS*, 378, 369
- Okuzumi, S. & Hirose, S. 2011, *ApJ*, 742, 65
- Owen, J. E. 2014, *ApJ*, 789, 590
- Papaloizou, J. C. B., Nelson, R. P., Kley, W., Masset, F. S., & Artymowicz, P. 2007, in *Protostars and Planets V*, ed. B. Reipurth, D. Jewitt, & K. Keil (Tucson: Univ. Arizona Press), 655
- Pérez, L. M., Isella, A., Carpenter, J. M., & Chandler, C. J. 2014, *ApJ*, 783, L13
- Piétu, V., Guilloteau, S., & Dutrey, A. 2005, *A&A*, 443, 945
- Pineda, J. E., Quanz, S. P., Meru, F., Mulders, G. D., Meyer, M. R., Panić, O., & Avenhaus, H. 2014, *ApJ*, 788, 34
- Pinilla, P., Benisty, M., & Birnstiel, T. 2012a, *A&A*, 545, A81
- Quanz, S. P., Avenhaus, H., & Buenzli, E. et al. 2013, *ApJ*, 766, L2
- Racine, R., Walker, G. A. H., Nadeau, D., Doyon, R., & Marois, C. 1999, *PASP*, 111, 587
- Regály, Z., Juhász, A., Sándor, Z., & Dullemond, C. P. 2012, *MNRAS*, 419, 1701
- Regály, Zs., Király, S., & Kiss, L. L. 2014, *ApJ*, 785, 31
- Riaud, P., Boccaletti, A., Baudrand, J., & Rouan, D. 2006, *A&A*, 458, 317
- Rice, W. K. M., Armitage, P. J., Wood, K., & Lodato, G. 2006, *MNRAS*, 373, 1619
- Sano, T., Miyama, S. M., Umebayashi, T., & Nakano, T. 2000, *ApJ*, 543, 486
- Sault, R. J., Teuben, P. J., & Wright, M. C. H. 1995, *ASP Conf. Ser. 77, Astronomical Data Analysis Software and Systems IV*, ed. R. A. Shaw, H. E. Payne, & J. J. E. Hayes (San Francisco, CA: ASP), 433
- Strom, K. M., Strom, S. E., Edwards, S., Cabrit, S., & Skrutskie, M. F. 1989, *AJ*, 97, 1451
- Takami, M., Hasegawa, Y., & Muto, T. et al. 2014, *ApJ*, 795, 71
- Tang, Y.-W., Guilloteau, S., & Piétu, V. et al. 2012, *A&A*, 547, A84
- Terquem, C. E. J. M. L. J. 2008, *ApJ*, 689, 532
- Thalmann, C., Grady, C. A., & Goto, M. et al. 2010, *ApJ*, 718, L87
- Tsukagoshi, T., Momose, M., & Hashimoto, J. et al. 2014, *ApJ*, 783, 90
- van der Marel, N., van Dishoeck, E. F., & Bruderer, S. et al. 2013, *Sci*, 340, 1199
- Varnière, P. & Tagger, M. 2006, *ã*, 446, L13
- Verhoeff, A. P., Min, M., & Pantin, E. et al. 2011, *A&A*, 528, A91
- Williams, J. P. & Cieza, L. A. 2011, *ARA&A*, 49, 67
- Whitney, B. A., Robitaille, T. P., & Bjorkman, J. E. et al. 2013, *ApJS*, 207, 30
- Wood, K., Wolff, M. J., Bjorkman, J. E., & Whitney, B. 2002, *ApJ*, 564, 887
- Zhu, Z., Nelson, R. P., Hartmann, L., Espaillat, C., & Calvet, N. 2011, *ApJ*, 729, 47
- Zhu, Z., Nelson, R. P., Dong, R., Espaillat, C., & Hartmann, L. 2012, *ApJ*, 755, 6
- Zhu, Z., Stone, J. M., Rafikov, R. R. & Bai, X. 2014, *ApJ*, 785, 122
- Zhu, Z. & Stone, J. M. 2014, *ApJ*, 795, 53

TABLE 1  
PDS 70 OBSERVATIONS

Date	Configuration	Number of Antennas	Beam Size	SSB $T_{sys}$ (K)	LO frequency (GHz)
2012 Dec 13	Compact	7	$3''.0 \times 6''.3$	170-200	225.507
2013 Apr 15	Compact	7	$5''.7 \times 3''.0$	170-350	225.501
2012 Dec 27	Extended	7	$1''.8 \times 1''.0$	230-360	225.227
2013 Jan 03	Extended	7	$1''.8 \times 1''.0$	140-200	225.230
2013 Feb 04	Very extended	8	$0''.9 \times 0''.4$	85-120	224.859

TABLE 2  
PARAMETERS IN OUR FIDUCIAL MODEL AND PREVIOUS MODEL

(Column 1)	(2)	(3)	(4)	(5)	(6)	(7)	(8)	(9)	(10)	(11)
Model	$M_{\text{disk}}$ ( $M_{\text{Jup}}$ )	$f$	$R_{\text{c}}$ (AU)	$R_{\text{gap}}^{\text{l}}$ (AU)	$R_{\text{gap}}^{\text{s}}$ (AU)	$h_{100\text{AU}}^{\text{l}}$ (AU)	$h_{100\text{AU}}^{\text{s}}$ (AU)	$p$	$q$	$\delta$
This work	4.5	0.9667	20	80	65	2.00	8.00	1.25	1.00	$10^{-4}$
Previous work	3.0	0.9667	50	65	65	2.00	10.00	1.20	1.00	$10^{-3}$

NOTE. — Column 2: total mass of the disk (assuming a gas-to-dust ratio 100). Column 3: mass fraction of big dust in total dust. Column 4: characteristic radius in equation 2. Column 5 and 6: gap-radius of the disk in large and small dust grains. Superscripts ‘l’ and ‘s’ indicate large and small dust grains, respectively. Column 7 and 8: scale height at 100 AU. Column 9: power index  $p$  in the scale height  $h \propto R^p$ . Column 10: power index in the surface density in equation 2. Column 11: depletion factor of the large and small dust disk.

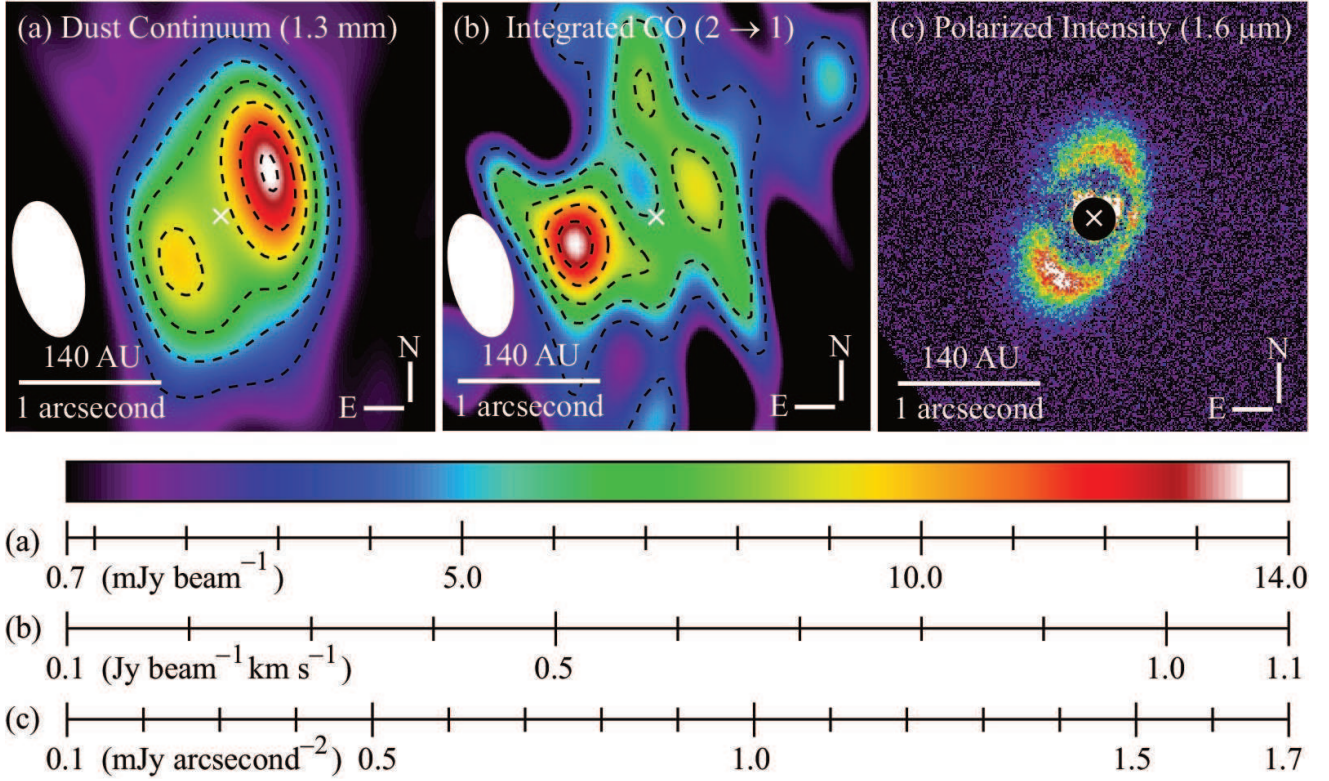


FIG. 1.— Observational results of PDS 70. (a): The dust continuum image at 1.3 mm. The beam size is  $0''.97 \times 0''.48$  at PA =  $12.33^\circ$  in the natural weight. Contours indicate 8, 14, 20, 26, 32, and 38  $\sigma$  ( $1 \sigma = 0.35 \text{ mJy beam}^{-1}$ ). (b): The integrated  $^{12}\text{CO}$  ( $2 \rightarrow 1$ ) emission image. The beam size is  $0''.88 \times 0''.43$  at PA =  $13.41^\circ$  in the natural weight. Contours indicate 2, 3, 4, 5, and 6  $\sigma$  ( $1 \sigma = 162.5 \text{ mJy km s}^{-1} \text{ beam}^{-1}$ ). (c): The  $1.6 \mu\text{m}$  polarized intensity image at the spatial resolution of  $\sim 0''.1$  (Hashimoto et al. 2012). Central region with a radius of  $0''.1$  is masked due to the dominant stellar photon noise. Crosses in each panels represent the astrometric point (14:08:10.125,  $-41:23:52.81$ ; Cutri et al. 2013).

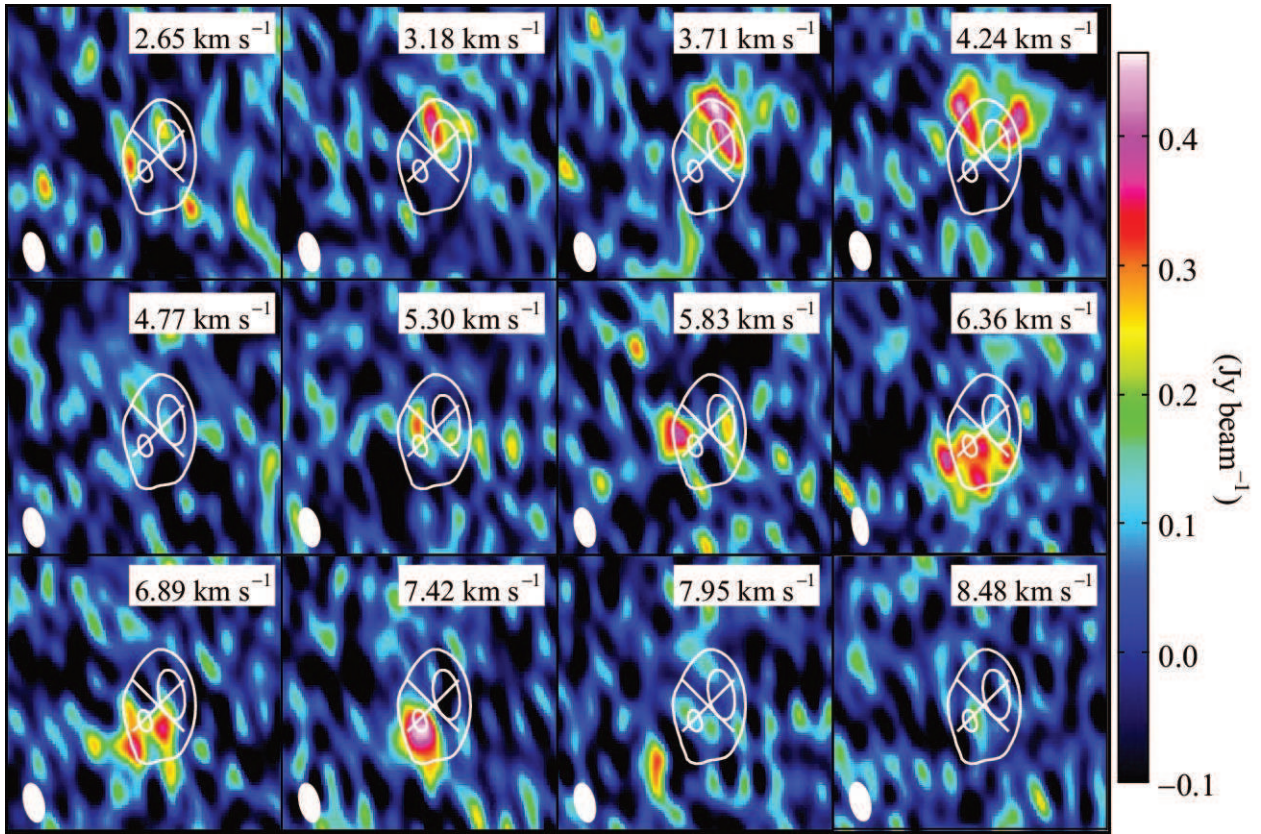


FIG. 2.— Channel maps of  $^{12}\text{CO}$  ( $2 \rightarrow 1$ ) line emission with natural weighting in the velocity range between 2.65 and 8.48  $\text{km s}^{-1}$ . The contours indicate the dust continuum in Fig. 1(a) with 8 and 26  $\sigma$  ( $1 \sigma = 0.35 \text{ mJy beam}^{-1}$ ). The synthesized beam is shown at the lower-left corner in each panel with  $0''.88 \times 0''.43$  at  $\text{PA} = 13.41^\circ$ . Crosses in each panels represent the astrometric point (14:08:10.125,  $-41:23:52.81$ ; Cutri et al. 2013).

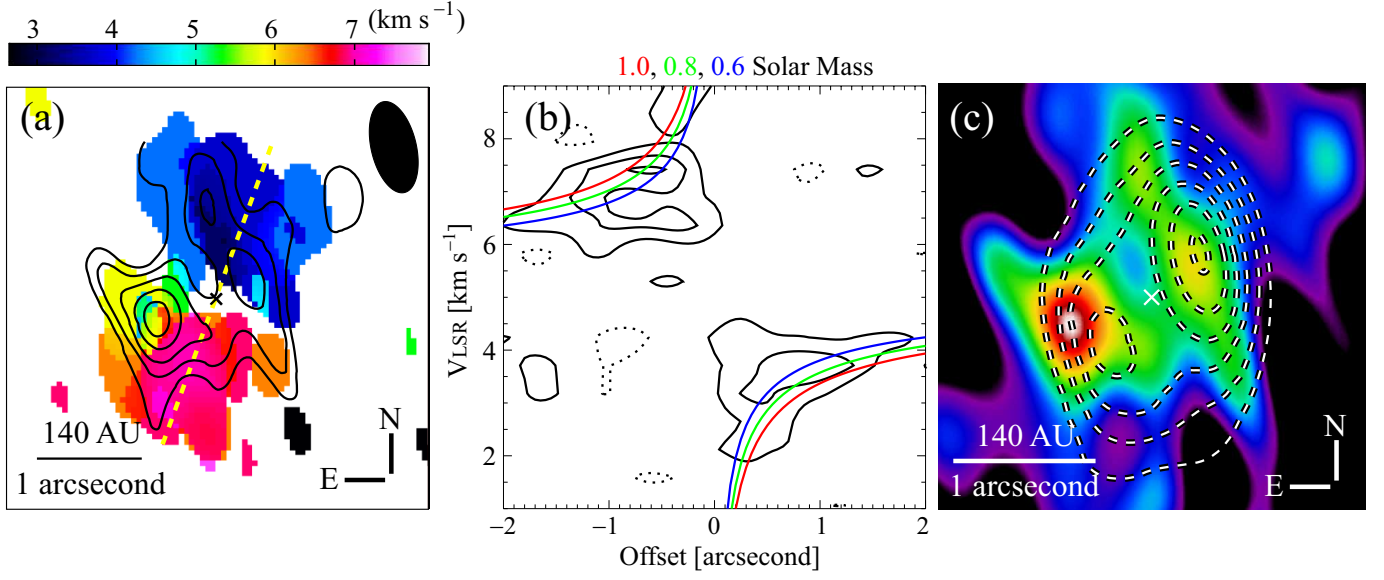


FIG. 3.— Observational results of  $^{12}\text{CO}$  ( $2 \rightarrow 1$ ) line emission of PDS 70. (a): Moment map with contours of the integrated  $^{12}\text{CO}$  ( $2 \rightarrow 1$ ) emission (taken from Fig. 1b; the beam size of  $0''.88 \times 0''.43$  at  $\text{PA} = 13.41^\circ$ ). (b): Position-velocity diagram along the yellow dashed-line ( $\text{PA} = 160^\circ$ ; centered at the astrometric point) in panel (a). The disk inclination is set to  $50^\circ$  taken from Hashimoto et al. (2012). Colored thick-lines are loci of peak emission in the Keplerian disk around the central star with a mass of 1.0 (red), 0.8 (green), and  $0.6 M_\odot$  (blue). Black contours are spaced by  $2 \sigma = 0.07 \text{ Jy beam}^{-1}$ . (c): The integrated  $^{12}\text{CO}$  ( $2 \rightarrow 1$ ) emission-line image with contours of the dust continuum taken from Fig. 1(a) and (b). Crosses in panels (a) and (c) represent the astrometric point (14:08:10.125,  $-41:23:52.81$ ; Cutri et al. 2013).

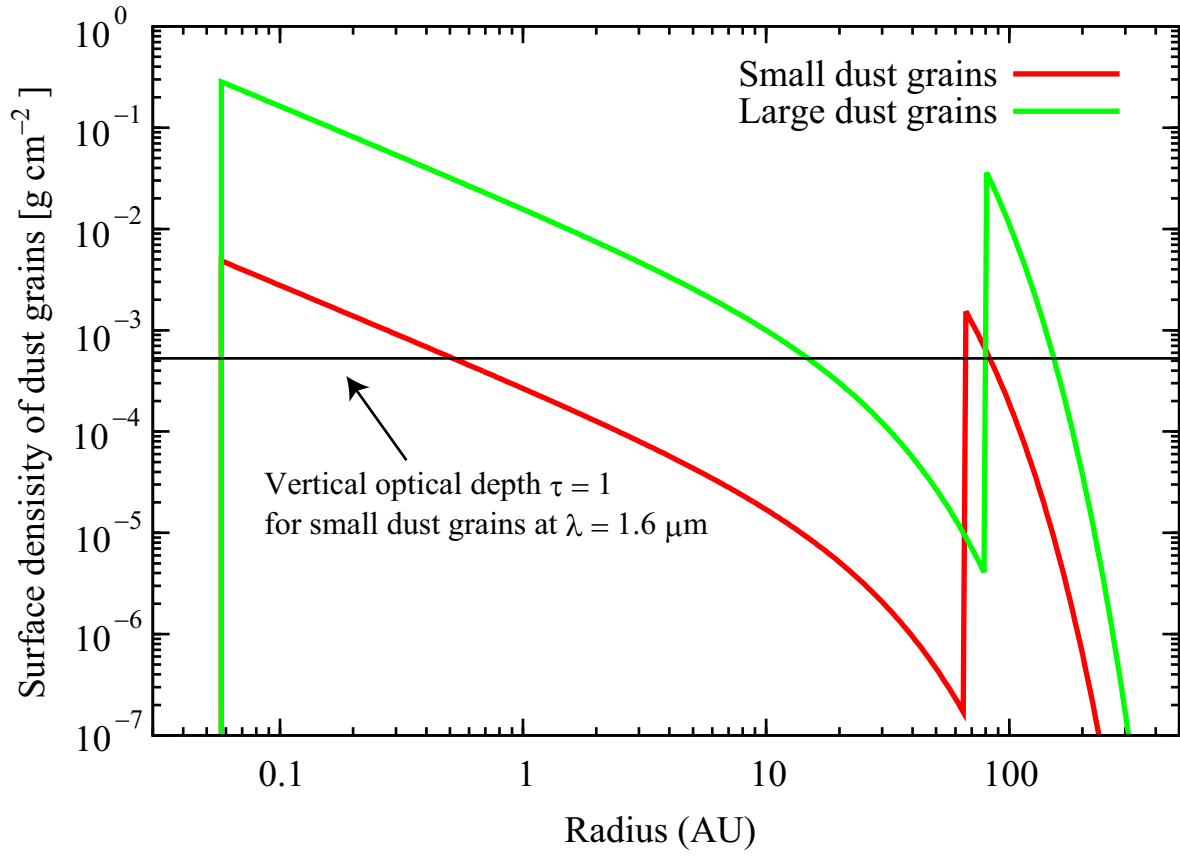


FIG. 4.— A surface density of small and large dust grains in our fiducial model.



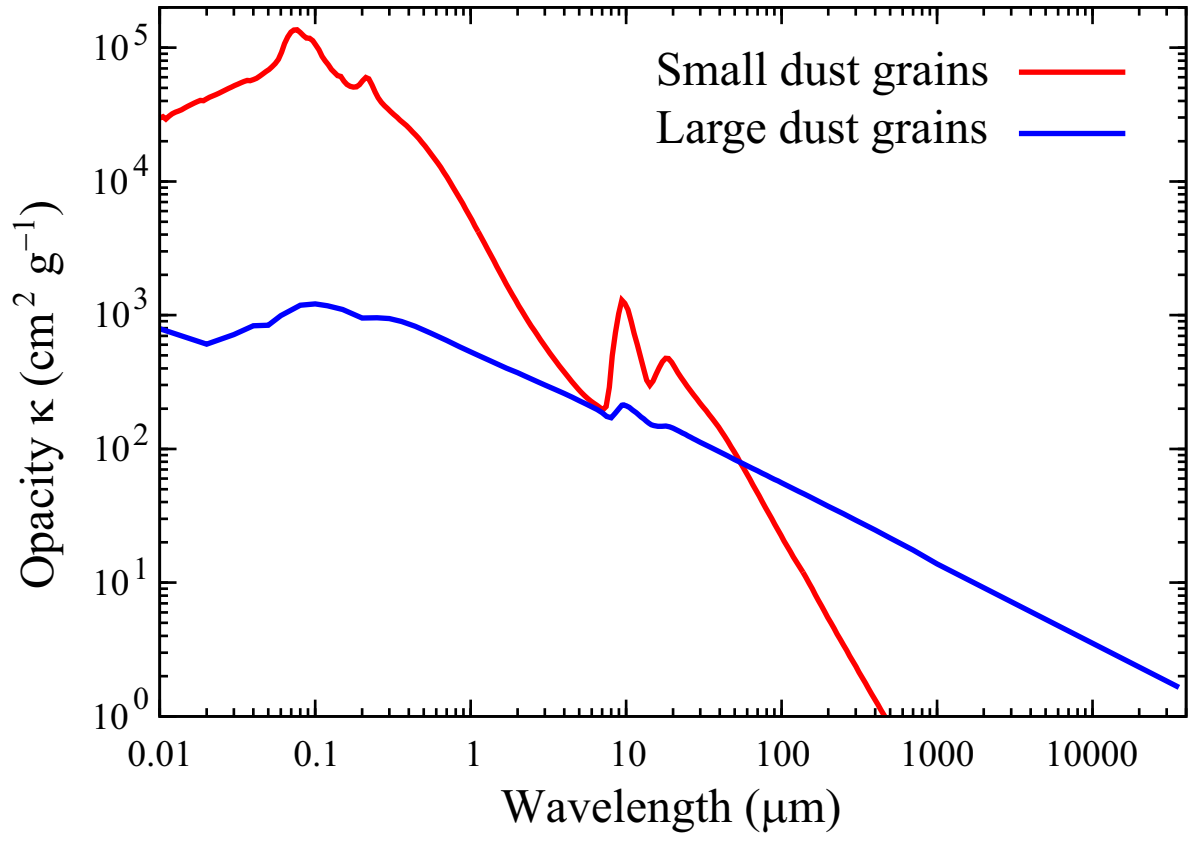


FIG. 5.— Opacity of small and large dust grains used in our modeling efforts.

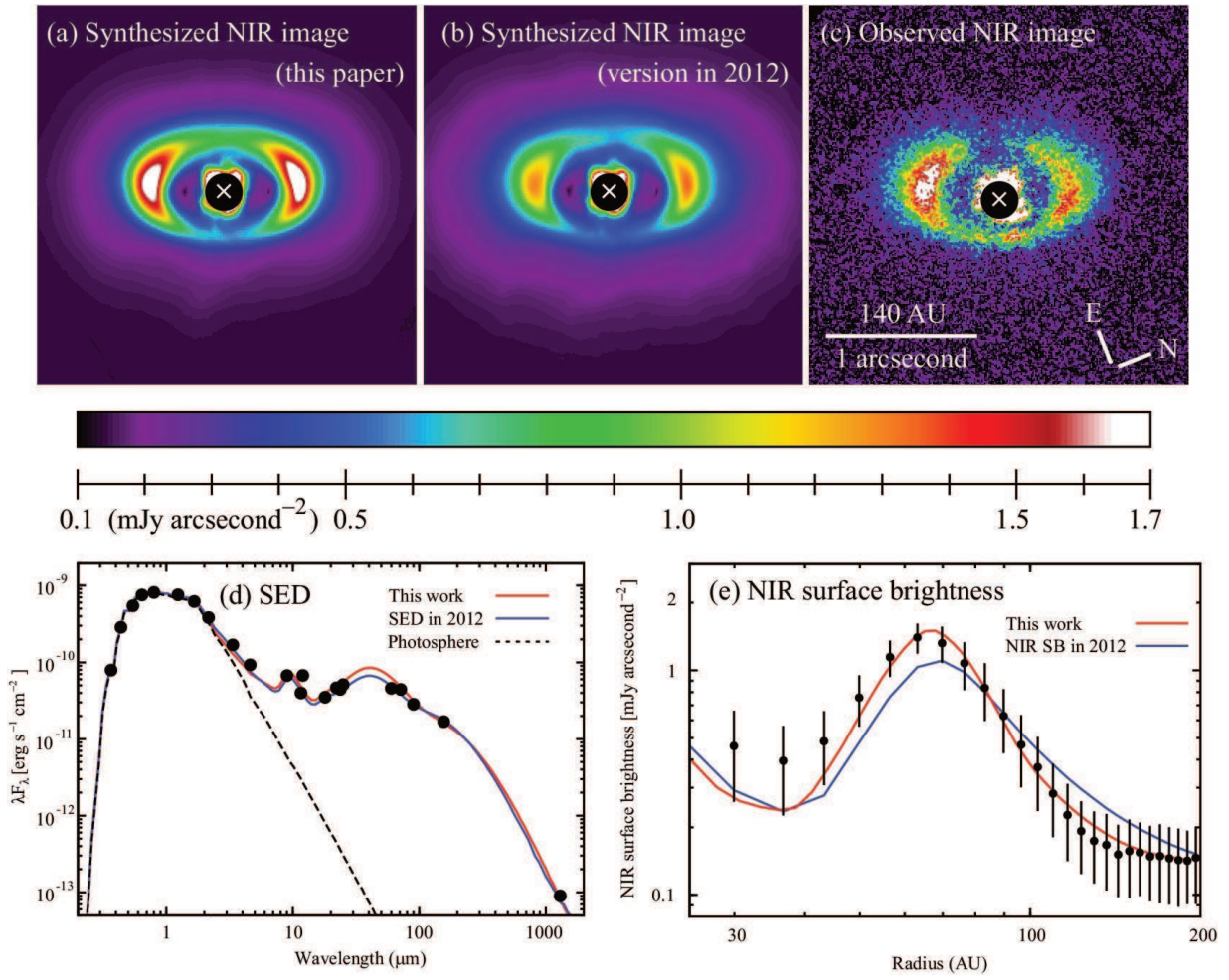


FIG. 6.— Comparisons of the synthesized NIR polarized intensity images in our fiducial model and previous model. (a) and (b): The synthesized images in our fiducial model and previous model, and (c): NIR observational results in Fig. 1(c). Crosses represent the astrometric point (14:08:10.125,  $-41:23:52.81$ ; Cutri et al. 2013). The synthesized images in panel (a) and (b) are processed with subtracting the polarized halo and adding the offset value (see § 3.2). (d): The synthesized SED and (e): radial profiles along the major axis in panel (a) and (b). Note that error bars in the SED are smaller than plots.

## Synthesized dust continuum at 1.3 mm

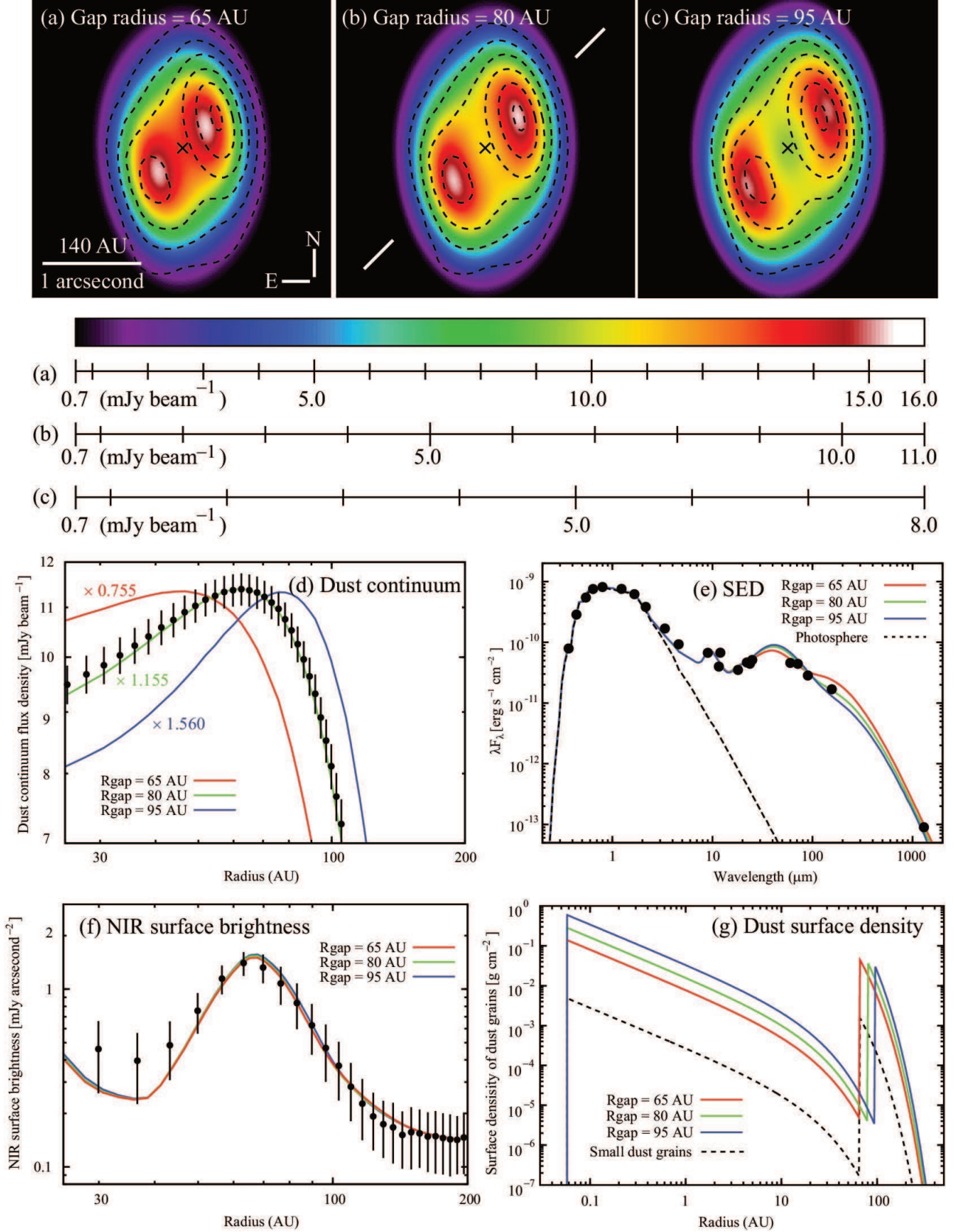


FIG. 7.— Our modeling efforts in synthesizing the dust continuum, the SED, and the NIR polarized-intensity surface brightness. (a) to (c): the synthesized dust continuum images varying a radius of a gap in large dust grains (65, 80, and 95 AU). A gap-radius in small dust grains is set to 65 AU and other parameters follow those in the fiducial model listed in table 2. Contours are taken from our SMA observations and same with Fig. 1(a). (d): The radial profile of the synthesized dust continuum at  $\text{PA} = 135^\circ$  (along a white line in panel b), (e): the synthesized SED, (f) the radial profile of the NIR polarized-intensity surface brightness at  $\text{PA} = 160^\circ$ , and (g): the surface density used in our modeling efforts. Colored solid-lines indicate results of gap-radii in large dust grains of 65 (red), 80 (blue), and 95 AU (green). In panel (d), the flux densities of the synthesized dust continuum with gap-radii of 65, 80, and 95 are multiplied by 0.755, 1.155, and 1.560, respectively, for the presentation purpose. In panel (e), error bars in the SED are smaller than plots.